

Mesoscale Convective Vortices in Multiscale, Idealized Simulations: Dependence on Background State, Interdependency with Moist Baroclinic Cyclones, and Comparison with BAMEX Observations

ROBERT J. CONZEMIUS

Department of Atmospheric Science, Colorado State University, Fort Collins, Colorado, and WindLogics, Inc., Grand Rapids, Minnesota

MICHAEL T. MONTGOMERY

Department of Atmospheric Science, Colorado State University, Fort Collins, Colorado, and Naval Postgraduate School, Monterey, California

(Manuscript received 3 March 2009, in final form 17 October 2009)

ABSTRACT

A set of multiscale, nested, idealized numerical simulations of mesoscale convective systems (MCSs) and mesoscale convective vortices (MCVs) was conducted. The purpose of these simulations was to investigate the dependence of MCV development and evolution on background conditions and to explore the relationship between MCVs and larger, moist baroclinic cyclones. In all experiments, no mesoscale convective system (MCS) developed until a larger-scale, moist baroclinic system with surface pressure amplitude of at least 2 hPa was present. The convective system then enhanced the development of the moist baroclinic system by its diabatic production of eddy available potential energy (APE), which led to the enhanced baroclinic conversion of basic-state APE to eddy APE. The most rapid potential vorticity (PV) development occurred in and just behind the leading convective line. The entire system grew upscale with time as the newly created PV rotated cyclonically around a common center as the leading convective line continued to expand outward. Ten hours after the initiation of deep moist convection, the simulated MCV radii, heights of maximum winds, tangential velocity, and shear corresponded reasonably well to their counterparts in BAMEX. The increasing strength of the simulated MCVs with respect to larger values of background CAPE and shear supports the hypothesis that as long as convection is present, CAPE and shear both add to the strength of the MCV.

1. Introduction

The development of mesoscale convective vortices (MCVs) is one example of a process in which diabatic heating plays a central role in the intensification and maintenance of an atmospheric vortex (Fritsch et al. 1994; Raymond and Jiang 1990; Jiang and Raymond 1995; Houze 2004; Hertenstein and Schubert 1991; Davis and Weisman 1994). Using potential vorticity (PV) concepts, the intensification can be explained by the vertical gradient of diabatic heating within the convective system. Raymond and Jiang (1990) and Jiang and Raymond (1995) developed a nonlinear balance model using these

PV concepts to explore the relationship between the balanced circulation of the vortex and its interaction with the vertical shear in which the vortex resides. The same conceptual model has been invoked (Fritsch et al. 1994; Galarneau et al. 2009) to explain the persistence, cyclic redevelopment, and upscale growth of MCVs. In this model, vertical gradients of diabatic heating produce a PV maximum in the lower to mid troposphere overlain by a PV relative minimum near the tropopause. Although the PV structure resides in a layer of vertical shear (due to thermal wind balance) that would tend to destroy the vortex over time, the balanced cyclonic motion associated with the vortex brings about a region of warm, moist advection and lift on the downshear side of the vortex. The lift brings about further convection and diabatic heating that helps maintain the vortex in the face of the sheared environment.

Corresponding author address: Robert J. Conzemiuss, WindLogics, Inc., 201 NW 4th Street, Grand Rapids, MN 55744.
E-mail: robert.conzemiuss@att.net

Report Documentation Page

Form Approved
OMB No. 0704-0188

Public reporting burden for the collection of information is estimated to average 1 hour per response, including the time for reviewing instructions, searching existing data sources, gathering and maintaining the data needed, and completing and reviewing the collection of information. Send comments regarding this burden estimate or any other aspect of this collection of information, including suggestions for reducing this burden, to Washington Headquarters Services, Directorate for Information Operations and Reports, 1215 Jefferson Davis Highway, Suite 1204, Arlington VA 22202-4302. Respondents should be aware that notwithstanding any other provision of law, no person shall be subject to a penalty for failing to comply with a collection of information if it does not display a currently valid OMB control number.

1. REPORT DATE OCT 2009	2. REPORT TYPE	3. DATES COVERED 00-00-2009 to 00-00-2009			
4. TITLE AND SUBTITLE Mesoscale Convective Vortices in Multiscale, Idealized Simulations: Dependence on Background State, Interdependency with Moist Baroclinic Cyclones, and Comparison with BAMEX Observations		5a. CONTRACT NUMBER			
		5b. GRANT NUMBER			
		5c. PROGRAM ELEMENT NUMBER			
6. AUTHOR(S)		5d. PROJECT NUMBER			
		5e. TASK NUMBER			
		5f. WORK UNIT NUMBER			
7. PERFORMING ORGANIZATION NAME(S) AND ADDRESS(ES) Naval Postgraduate School, Department of Meteorology, Monterey, CA, 93943		8. PERFORMING ORGANIZATION REPORT NUMBER			
9. SPONSORING/MONITORING AGENCY NAME(S) AND ADDRESS(ES)		10. SPONSOR/MONITOR'S ACRONYM(S)			
		11. SPONSOR/MONITOR'S REPORT NUMBER(S)			
12. DISTRIBUTION/AVAILABILITY STATEMENT Approved for public release; distribution unlimited					
13. SUPPLEMENTARY NOTES					
14. ABSTRACT A set of multiscale, nested, idealized numerical simulations of mesoscale convective systems (MCSs) and mesoscale convective vortices (MCVs) was conducted. The purpose of these simulations was to investigate the dependence of MCV development and evolution on background conditions and to explore the relationship between MCVs and larger, moist baroclinic cyclones. In all experiments, no mesoscale convective system (MCS) developed until a larger-scale, moist baroclinic system with surface pressure amplitude of at least 2 hPa was present. The convective system then enhanced the development of the moist baroclinic system by its diabatic production of eddy available potential energy (APE), which led to the enhanced baroclinic conversion of basic-state APE to eddy APE. The most rapid potential vorticity (PV) development occurred in and just behind the leading convective line. The entire system grew upscale with time as the newly created PV rotated cyclonically around a common center as the leading convective line continued to expand outward. Ten hours after the initiation of deep moist convection, the simulated MCV radii, heights of maximum winds tangential velocity, and shear corresponded reasonably well to their counterparts in BAMEX. The increasing strength of the simulated MCVs with respect to larger values of background CAPE and shear supports the hypothesis that as long as convection is present, CAPE and shear both add to the strength of the MCV.					
15. SUBJECT TERMS					
16. SECURITY CLASSIFICATION OF:			17. LIMITATION OF ABSTRACT Same as Report (SAR)	18. NUMBER OF PAGES 21	19a. NAME OF RESPONSIBLE PERSON
a. REPORT unclassified	b. ABSTRACT unclassified	c. THIS PAGE unclassified			

The same PV concepts have been employed as a proposed mechanism for the initial development of moist baroclinic systems (Montgomery and Farrell 1991; Moore and Montgomery 2004, 2005, hereafter MM04 and MM05). In the moist baroclinic case, the diabatic heating commences in a region of lift well downshear from the initiating midlevel disturbance, and the initial vortex that develops is resistant to the effects of the shear because of the reinforcing effects of the latent heat release in clouds on its downshear side. MM05 coined the term “diabatic Rossby vortex” for such vortical disturbances, although in an earlier study Snyder and Lindzen (1991) referred to the wavelike counterparts as diabatic Rossby waves.

Whereas cold season baroclinic cyclones ultimately derive a majority of their energy from the available potential energy (APE) of the basic state (Davis et al. 1993), the diabatic production of PV can be a strong contributor to their development, especially over the oceans (Montgomery and Farrell 1992; Whitaker and Davis 1994; MM04; MM05; Moore et al. 2008). In warm season situations, the background APE may be somewhat less, but the convective instability also allows locally stronger diabatic heating; like their cold season counterparts, the warm season disturbances move along larger-scale temperature gradients. Additionally, MM04 show a region of scale independence of moist baroclinic growth below a certain horizontal wavelength, motivating an extension of these studies into environments, more typical of warm season conditions (Conzemius et al. 2007, hereafter C1) that allow the development of some CAPE.

In the idealized simulations of C1, it was found that the development of organized, deep, moist convection required the presence of larger-scale forcing. The development of the mesoscale convective system (MCS) occurred in conjunction with the deepening of the most rapidly growing moist baroclinic wave, regardless of any attempt to minimize the effects of the larger moist baroclinic system in the simulations. The overall conclusion was that an important scale interaction existed, in which the development of the MCS was dependent on the deep, persistent upward vertical motion and the moist, low-level inflow provided by the larger-scale system.

In the present study, another avenue we wish to explore is the reverse interaction—whether the MCVs have a direct feedback on the growth rate of synoptic-scale, baroclinic waves. Any vortex that has a localized distribution in physical space will project onto a spectrum of scales that will include large-scale baroclinic waves (C1), which may or may not be exponentially unstable. An MCV developing within a moist baroclinic system should be no exception. Additionally, the energy conversion calculations in C1 revealed that although the diabatic

production of eddy APE is a significant contributor to the net eddy APE, the conversion of mean state APE to eddy APE (baroclinic conversion) increased in tandem with the diabatic production of APE. This result suggests an important upscale feedback from the mesoscale (MCV/MCS) to synoptic scales in the development of moist baroclinic cyclones. Although less baroclinically unstable environments can be expected in the summer when MCVs are much more prevalent, it can still be expected that the MCVs play a role in the maintenance of synoptic-scale systems in the midlatitudes in summer, particularly since they often appear to undergo an upscale growth (Fritsch et al. 1994; C1; Galarneau et al. 2009). In more weakly sheared environments, there may also be some implications for the development and maintenance of easterly waves and the mesoscale convective systems embedded within them as recently hypothesized in the marsupial theory of tropical cyclogenesis (Dunkerton et al. 2008; see their hypothesis 3).

A second goal of the present study is to take a more detailed look at the PV development process and, in particular, the process by which the MCV grows upscale to the point that it becomes not easily distinguished from the developing moist baroclinic cyclone (Galarneau et al. 2009). One question that arises is whether or not the upscale growth occurs via diabatic production or via axisymmetrization of the PV.

In the spring and summer of 2003, the Bow Echo and Mesoscale Convective Vortex Experiment (BAMEX; Davis et al. 2004) took place with an aim to observe, on multiple scales, the process of MCV formation within MCSs. Although MCVs have historically been assumed to form primarily within environments where the shear is relatively small and dynamically of second order (Bartels and Maddox 1991; Cotton and Anthes 1989; Houze 2004), other studies have found them to form in both weakly and strongly sheared background environments (Trier et al. 2000; Davis et al. 2002). The more recent BAMEX data demonstrated MCVs to be present in both strong and weak deep-layer shear environments (Davis and Trier 2007). Given these results, a more complete understanding of the MCV problem with varying vertical shear seems highly warranted. Since the C1 study only covered background conditions of relatively modest shear, we seek here to extend the investigation using idealized simulations into more strongly sheared environments. For similar reasons, the investigations need to explore environments with larger CAPE. The recent results of Davis and Trier (2007), which examined MCV structure within environments of varying CAPE and shear, also naturally motivate us to determine whether similar structures can be simulated with similar antecedent conditions as in BAMEX.

2. Methods

The idealized simulations were constructed using the same basic methods as in MM05 and C1. A meridionally varying, Eady-type basic state was constructed, and the initial state of the simulation was created by inserting a low-level, warm-core vortex with zero interior PV anomalies into the basic state. The fifth-generation Pennsylvania State University–National Center for Atmospheric Research (NCAR) Mesoscale Model (MM5) was used to numerically integrate the initial state forward in time.

a. Basic-state description

In C1, the construction of the basic state started by specifying a zero surface pressure gradient and a surface meridional temperature gradient whose magnitude varied according to a Gaussian function of latitude centered on 45°N. This meridional temperature gradient was held constant with height in the troposphere, and thermal wind balance was used to construct the basic state zonal wind. These same methods are used in the present study.

Because the temperature lapse rate in a moist neutral vertical profile varies strongly as a function of temperature (because of the exponential dependence of saturation vapor pressure on temperature), C1 had to use a latitude-dependent LCL height to produce the Eady-type shear in the basic state. However, in the present study, the intent was to create a background environment of larger CAPE, so a constant temperature lapse rate of 8 K km⁻¹ was used above the PBL top throughout the tropospheric portion of the domain. To avoid convection initiating everywhere in the CAPE-laden portion of the domain, a temperature jump of 1.5 K and a dewpoint depression of 1.5 K were used at the top of the PBL. The PBL top was set to a constant value of 850 hPa in the entire domain. The potential temperature at the PBL top was the same as the surface potential temperature (i.e., a well-mixed PBL), and the mixing ratio was also held constant in the PBL. The PBL mixing ratio was calculated using the temperature and the dewpoint depression at the PBL top. An upper bound of 16 g kg⁻¹ was used to limit the CAPE in the basic state; with this limit, the magnitude of the PBL top dewpoint depression in the southern portion of the domain was larger than 1.5 K.

The tropopause pressure was allowed to vary meridionally in the shape of half the period of a sine function over the width of the baroclinic zone with the maximum slope at the center of the baroclinic zone (45°N). The total width of the baroclinic zone was 60 degrees latitude for most cases. The vertical profile of relative humidity was that of a hyperbolic tangent function with the humidity decreasing from its value at the top of the PBL

to 25% at the tropopause, and the stratospheric relative humidity was held constant at 25%. A sample sounding from the center of the baroclinic zone is shown in Fig. 1.

b. Experiments

We adopt a nomenclature for these simulations in the format CAccSHssBZww, where “cc” is the surface-based CAPE (through the rest of the document, we refer to CAPE as surface-based CAPE) in the center of the baroclinic zone (hundreds of J kg⁻¹), “ss” the shear in the basic state (tenths of m s⁻¹ km⁻¹) and “ww” the width of the baroclinic zone (degrees latitude). The format is designed to allow the reader to quickly identify the basic-state configuration during the results discussion.

Five separate basic-state configurations have been constructed for the exploration of the parameter space (see Table 1). The first is the configuration from C1 and is referred to as the CA00SH15BZ60 simulation. This simulation has a background profile that is neutral to the ascent of saturated parcels (i.e., moist adiabatic) and is the starting point for our exploration of the parameter space. The second basic state (CA22SH15BZ60) contains a steeper midlevel temperature lapse rate to allow larger CAPE in the initial state. It has 2200 J kg⁻¹ CAPE in the center of the baroclinic zone and the same shear as in the CA00SH15BZ60 experiment. To further explore the range of shear that has been observed in MCVs (Trier et al. 2000; Davis and Trier 2007), the third basic state (CA15SH30BZ60) has similarly large CAPE but twice the shear of the first two simulations. To keep the surface temperature in the southern portion of the domain within reasonable atmospheric limits, the central baroclinic zone temperature in the CA15SH30BZ60 simulations was set to 300 K, reducing the CAPE there to 1553 J kg⁻¹. Motivated by the small values of shear observed in BAMEX intensive observing period (IOP) 8 (Davis and Trier 2007), we also performed a simulation with half the shear of the CA00SH15BZ60 simulation but large CAPE (CA22SH08BZ60). Finally, a simulation with a narrower baroclinic zone was conducted (CA15SH30BZ30), the purpose of which was to mimic the more typical structure of warm season baroclinic zones, which are often latitudinally much narrower than their cold season counterparts. The narrower baroclinic zone would allow the MCV to move northward out of this zone more easily and thereby experience changes in forcing with regard to the thermal gradient and vertical shear. Additionally, we wished to reduce the CAPE to the north of the baroclinic zone since it appeared that in the other experiments, the CAPE there caused more widespread deep convective development than is typically found in observed systems.

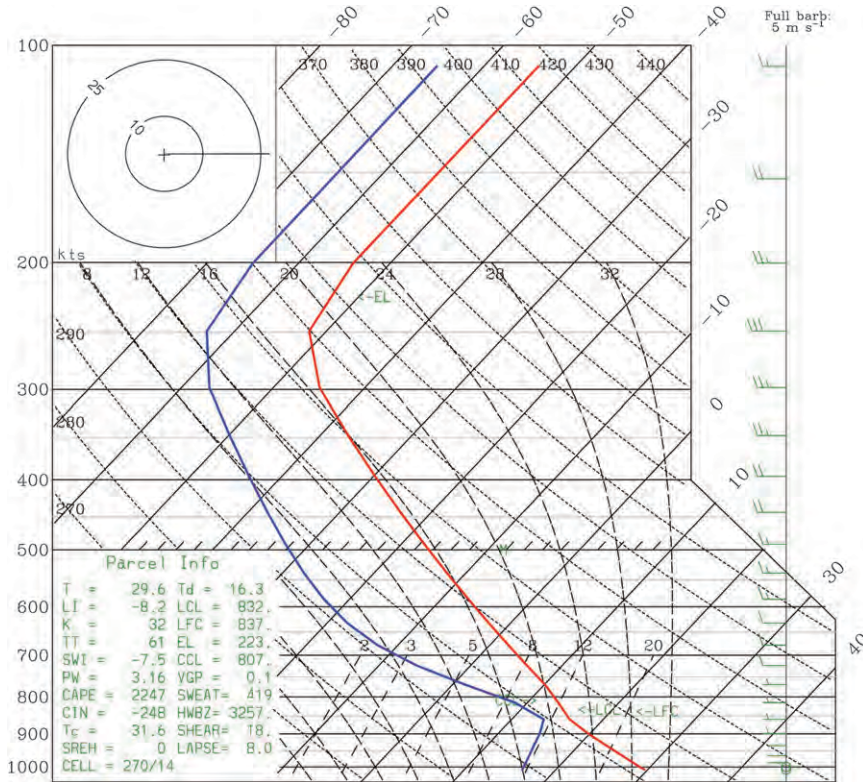


FIG. 1. Skew- T -log- p diagram in the center of the baroclinic zone (45°N) for the basic state of the CA22SH15BZ60 simulation (see Table 1).

c. Initial vortex

During the initial setup of the CA22SH15BZ60 simulation, the shape of the initial low-level vortex temperature perturbation was set to the second derivative of the Gaussian profile (the isolated vortex), with an e -folding radius of 300 km. The reason for doing so was to minimize the initial projection on the most rapidly growing and most baroclinic wavenumber. However, since the isolated initial radial profile only served to delay the MCS development relative to the simulations initialized with the Gaussian radial profile, all subsequent simulations were initialized with the Gaussian vortex, as described in C1.

d. MM5 setup

MM5 is a limited-area, nonhydrostatic, terrain-following, sigma-coordinate numerical model. Grell et al. (1994) provide a complete description of MM5. For each experiment, a coarse-resolution simulation was first performed using a 90-km domain with a size of approximately 12 000 km \times 5000 km in the zonal and meridional directions, respectively, and 23 vertical levels. The coarse-resolution simulation settings included full Coriolis force, the simple ice (Dudhia) moisture scheme, the Grell et al. (1994) cumulus parameterization, and the Medium-Range Forecast (MRF) model boundary layer parameterization. The lateral boundary condition for all runs was that

TABLE 1. Selected parameters for basic state configuration.

	T_{cent} (K)	Shear _{cent} ($\text{m s}^{-1} \text{ km}^{-1}$)	Width _{BZ} ($^{\circ}$)	CAPE _{cent} (J kg^{-1})	CAPE _{max} (J kg^{-1})
CA00SH15BZ60	293	1.5	60	0	0
CA22SH15BZ60	303	1.5	60	2247	4200
CA15SH30BZ60	300	3.0	60	1553	4000
CA15SH30BZ30	300	3.0	30	1553	4100
CA22SH08BZ60	303	0.75	60	2247	4100

TABLE 2. Parameters of inner domains.

Simulation	Inner domain start time (h)	Move frequency (h)		Grid dimensions*		
		Grid 3	Grid 4	Grid 2	Grid 3	Grid 4
CA00SH15BZ60	120	—	24	94 × 76	229 × 172	271 × 211
CA22SH15BZ60	120	72	8	154 × 94	289 × 199	289 × 253
CA15SH30BZ60-1	42	24	8	211 × 109	286 × 286	286 × 286
CA15SH30BZ60-2	72	24	8	211 × 109	286 × 286	286 × 286
CA15SH30BZ30	24	24	8	211 × 109	286 × 286	286 × 286
CA22SH08BZ60	192	—	24	211 × 109	286 × 286	286 × 286

* Grids 2, 3, and 4 are the 30-, 10-, and 3.3-km grids, respectively.

of the basic-state environment. As in C1, the surface fluxes of latent and sensible heat as well as radiative processes were neglected, but the surface flux of momentum was retained.

The coarse-resolution simulation was integrated forward in time to provide an estimate of when deep convection might initiate. This estimate was then used for purposes of guiding the placement and movement of finer-resolution grids for a second, higher-resolution simulation. To provide for a near-cloud-resolving simulation of the convective processes associated with the MCV growth, three inner nested domains were used with grid intervals of 30, 10, and 3.3-km. While the finest grid interval of 3.3 km is not expected to fully represent processes on the cloud scale (Bryan et al. 2003), we expect to resolve those processes that are essential to the generation of MCVs. The Grell et al. (1994) cumulus parameterization was used on the 90-, 30-, and 10-km domains but turned off in the 3.3-km grid. The MRF PBL scheme was used on the 30-km domain, and the Blackadar PBL scheme was used on the 10- and 3.3-km domains.

In this finer-resolution simulation, the inner grids were initialized when a contiguous area of convective accumulated precipitation developed in the coarse-resolution simulation, grew over at least two consecutive 12-h intervals (e.g., 12 h, 24 h, 36 h, etc.), and reached values of at least 5 mm. The inner grids were then turned on at the beginning of the nearest 6-h period prior to this onset. For example, if persistent, convective accumulated precipitation was first observed at $t = 48$ h in the simulation, the inner grids were initialized at $t = 42$ h in the finer-resolution simulation.

Because of the varying conditions of shear and CAPE, it was necessary to move the innermost two domains at different intervals for each experiment as indicated in Table 2. The simulation was integrated forward in time until the convective system grew beyond the bounds of the 3.3-km domain.

e. Dry simulations

In addition to the experiments above, we conducted several dry simulations to investigate the effect of the

latent heating, provided by the convective development, on the moist baroclinic system. In these simulations, the corresponding moist case was run long enough for the deep convection to initiate, the data were saved, and then the runs restarted with the latent heating turned off. For the CA22SH15BZ60 simulation, a dry restart was also performed several hours before the initiation of deep, moist convection. A summary of the dry runs is provided in Table 3.

f. Analysis tools

1) ENERGY CONVERSION CALCULATIONS

As in C1, we calculated the diabatic (G_E) and baroclinic (C_A) conversion terms to compare the energetics of the CA00SH15BZ60 and CA22SH15BZ60 simulations. These conversion terms represent the baroclinic conversion of mean-state APE and the diabatic conversion of latent heat energy, respectively, to eddy APE. The terms are defined by the following formulas (Norquist et al. 1977):

$$G_E = \int_{p_1}^{p_2} \frac{\overline{Q'T'}}{c_p \bar{\sigma}} dp, \quad (1)$$

$$C_A = - \int_{p_1}^{p_2} \frac{\overline{v'T'} \partial[T]}{\bar{\sigma} \partial y} dp - \int_{p_1}^{p_2} \frac{\overline{\omega'T'} \partial[T]^*}{\bar{\sigma} \partial p} dp, \quad (2)$$

where $[\langle \cdot \rangle]$ represents a zonal average of the quantity (\cdot) and $\overline{[\langle \cdot \rangle]}$ represents an area mean. A prime indicates the deviation from the zonal average, and an asterisk indicates a deviation of the zonal average from the area mean; Q is the diabatic heating rate ($\text{J kg}^{-1} \text{s}^{-1}$), T is temperature, c_p is the heat capacity at constant pressure

TABLE 3. Restart times for the dry simulations.

Experiment	Restart time (h)	Time relative to deep convection initiation (h)
CA22SH15BZ60	140	-10
CA22SH15BZ60 (second dry)	160	10
CA15SH30BZ30	48	4

for dry air ($\text{J kg}^{-1} \text{K}^{-1}$), and σ is the area-average static stability, where

$$\bar{\sigma} = g \left(\frac{[\overline{T}]}{c_p} - \frac{p}{R} \frac{\partial [\overline{T}]}{\partial p} \right);$$

also, v is the meridional component of velocity, ω is the vertical velocity in pressure coordinates, and p_1 and p_2 are the pressure limits of integration.

We conducted a limited area analysis on the 90-km domain, centered on the surface pressure minimum, and extending 15° of longitude (approximately 1350 km) east and west of the minimum and 10° (approximately 900 km) north and south of the minimum. The analysis was performed on the 90-km domain in order to encompass the entire large-scale system.

2) VERTICAL SHEAR ANALYSIS

Using the method outlined in Davis and Trier (2007), we calculated the area average of 1–4 and 1–8 km vertical shear within 300 km of the MCV center. We performed the calculations on the 30-km domain and defined the MCV center to be the location of the minimum 700-hPa geopotential height perturbation from the zonal average. The zonal and meridional wind components u and v at 1, 4, and 8 km AGL were horizontally averaged over an area within 300 km radius of the center. The vector differences among these horizontal averages were then calculated.

3. Results

The timeline on which we present the results of the simulations begins upon the initiation of deep moist convection and lasts for 40 h after initiation. We identify the initiation to be the time when the first model-derived reflectivity greater than 5 dBZ appears at the 700-hPa level, followed by growth to become an MCS.

a. General overview of simulations

Initiation of deep moist convection in the CA22SH15BZ60 simulation occurs approximately 150 h into the simulation. Two hours later (Fig. 2a), the convection has grown into a small convective cluster. Six hours after initiation (Fig. 2b), a rather symmetric MCS has formed, featuring enhanced 700-hPa rear inflow along 52°N and a leading convective line spreading in a horseshoe pattern around this rear inflow. An area of stratiform precipitation is developing from the rear inflow into the center of the MCS. It is in Fig. 2b that the cyclonic circulation in the northern portion of the MCS starts to become visible. Four hours later (Fig. 2c), a well-developed MCV is present in the stratiform precipitation

area behind the leading convective line. This leading line extends southwestward from the developing circulation but also wraps cyclonically around the north side of the circulation. Eighteen hours after initiation (Fig. 2d), the same basic structure is present, but it has grown upscale to the point that the convection has expanded outside of the 3.3-km grid. The aerial extent of the 700-hPa circulation has grown beyond the limits of the innermost grid.

A look at larger scales (Fig. 3) reveals a close association between the MCS and a deepening moist baroclinic cyclone. The development of deep, moist convection occurs just to the east of the surface pressure minimum (Fig. 3a), which is a location favored for organized, persistent lifting motion in moist baroclinic cyclones (Bluestein 1992; Holton 2004). Ten hours after initiation, the large-scale cyclone is deepening, and the MCS is spreading outward around the center of the cyclone and along the leading edge of its expanding cold pool. The lack of surface fluxes in the simulations allows the cold pool development to be readily seen. For the next 20 h (Figs. 3c and 3d), the surface pressure minimum continues to deepen as the MCS spreads at the leading edge of its cold pool and also wraps cyclonically around the surface low. Thirty hours after initiation (Fig. 3d), a substantial portion of the convection is located to the north of the surface low. This location is influenced by the presence of moderate CAPE in the initial state north of the center of the baroclinic zone, and it may be considered rather atypical of real atmospheric MCS evolution. This result motivated us to carry out additional experiments with a narrower baroclinic zone and less CAPE to the north of the center of the baroclinic zone. The narrower baroclinic zone provides conditions more typical of the warm season with less basic-state APE.

An examination of the 2-m temperature and surface pressure evolution prior to initiation (not shown) reveals that the MCS is forced not by the warm core vortex but by the subsequent, larger-scale baroclinic wave excited by the initial vortex. The larger-scale development has a wavelength of roughly 3000 km, determined by measuring the half-wave distance from the surface pressure minimum to the downstream surface pressure maximum (Fig. 3a). Based on the parameters in the center of the baroclinic zone of the basic state of the simulation (see Fig. 1), we calculated the Rossby deformation radius NH/f (where N is the Brunt–Väisälä frequency, $H = 6000$ m is the scale height of the atmosphere, and f the Coriolis parameter) to be 700 km. The scale of development is therefore within the fast-growing, smaller wavenumber portion of the large cyclone growth regime presented in Fig. 1 of MM04.

The importance of the larger, baroclinic system is underscored by the fact that in every experiment, the

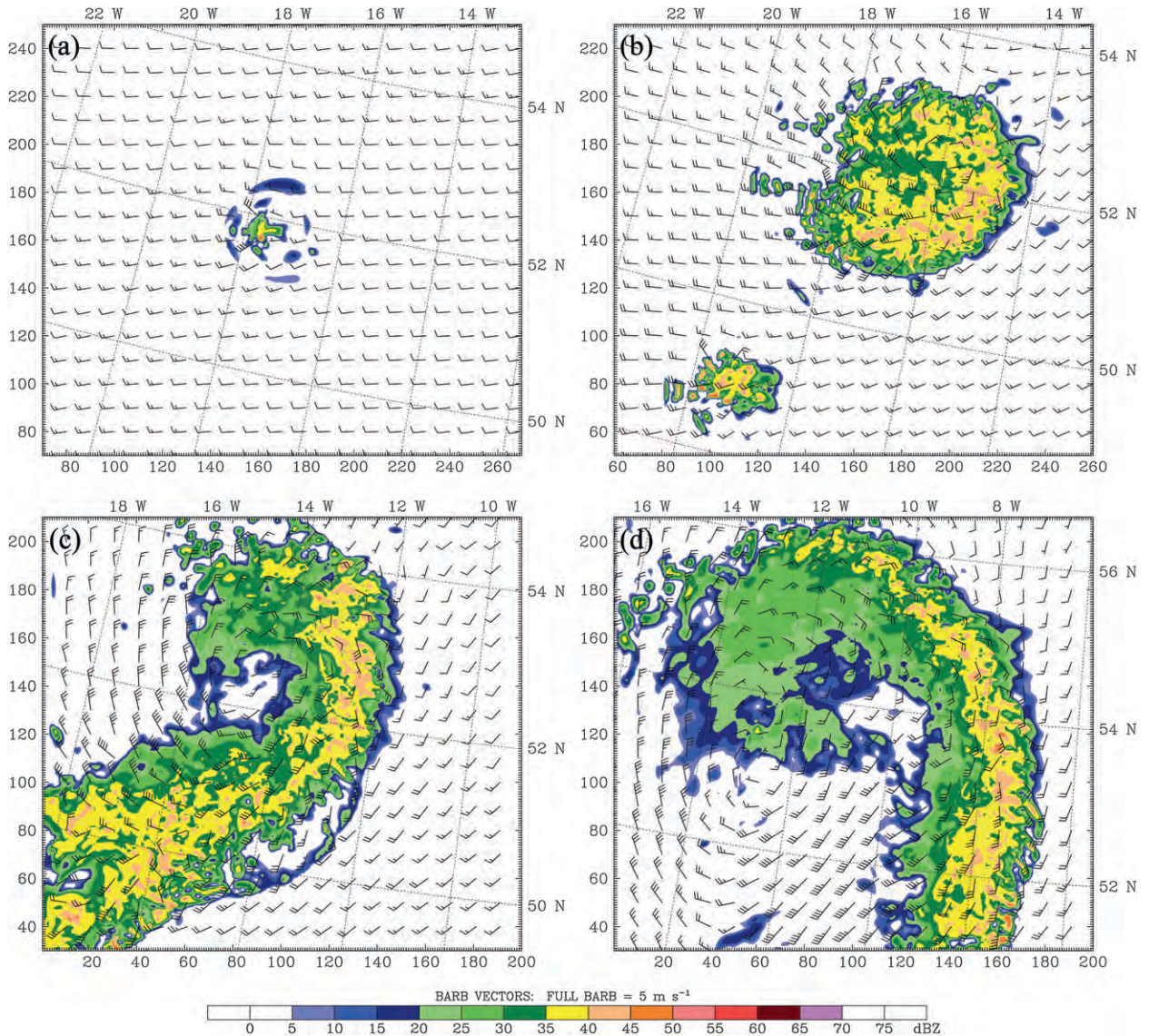


FIG. 2. Model-derived reflectivity (dBZ; shading) and horizontal flow (wind barbs; full barb = 5 m s^{-1}) at 700 hPa on the 3.3-km grid at the following times relative to initiation of deep convection in the CA22SH15BZ60 simulation: (a) 2, (b) 6, (c) 10, and (d) 18 h. The top and right axes indicate longitude and latitude, respectively; the bottom and left axes indicate grid indices on the 3.3-km domain. The equivalent radar reflectivity factor for rain Z_e ($\text{mm}^6 \text{ m}^{-3}$) is computed following Fovell and Ogura (1988) as $Z_e = 720\alpha k N_o \lambda^{-7} (\rho/\rho_w)^2$, where α is the nondimensional ratio of backscattering for the reflecting substance (1 for water, 0.213 for ice), $k = 10^{18}$ is the conversion factor from m^6 to the units of Z_e , N_o is the intercept parameter of the raindrop size distribution, ρ the density of the substance of interest (water or ice; ρ_w is the density of water), and λ is the slope of the raindrop size distribution: $\lambda = (\pi\rho_w N_o / \rho_a q_{ra})^{1/4}$, where ρ_a is the density of dry air and q_{ra} the rainwater mixing ratio. The reflectivity is expressed in decibels, or dBZ, where $\text{dBZ} = 10 \log_{10}(Z_e)$.

MCS development occurs just to the east of a minimum in surface pressure (Fig. 4). The location, in every circumstance of initiation, is in the typically favored area for lift, east of the surface low, where the large-scale flow induces relatively strong and persistent low-level frontogenesis (Bluestein 1992; Hoskins 1976). In the CA00SH15BZ60 simulation (Fig. 4a), initiation occurs at the north end of this zone at a location that has CAPE of only 300 J kg^{-1} .

In this experiment, the surface low development is collocated with the initial perturbation vortex.

In the CA22SH15BZ60 simulation (Fig. 4b), the frontogenesis is somewhat stronger, and at the point of initiation, CAPE is 2200 J kg^{-1} . Farther east of the surface low, around 11°W , is a second maximum in CAPE that is a remnant from the initial perturbation vortex. No MCS ever forms near this second maximum. A second

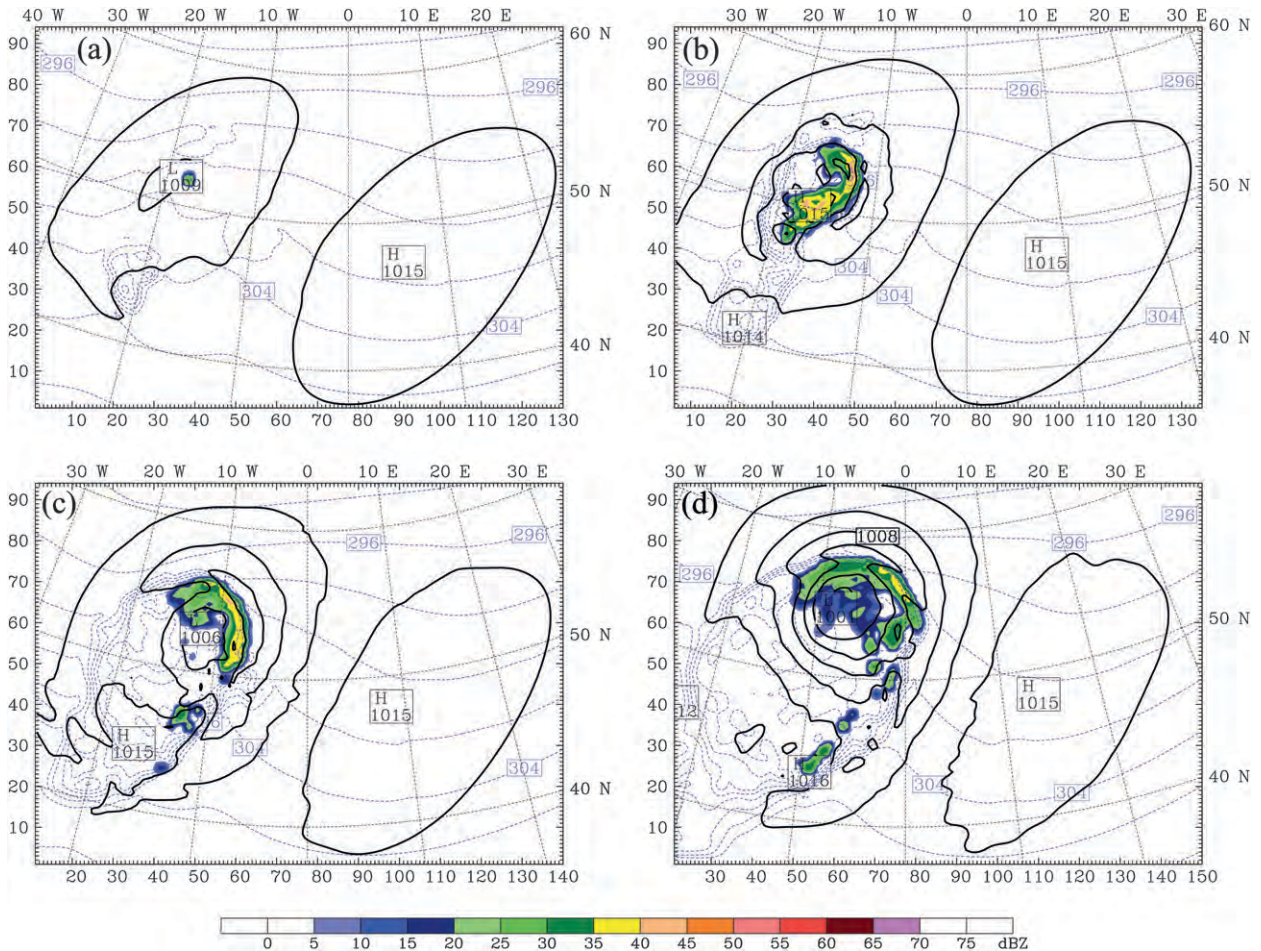


FIG. 3. Sea level pressure (black lines; contour interval 2 hPa), 2-m temperature (blue dashed lines; contour interval 2 K), and model-derived reflectivity (dBZ; shading) on the 30-km grid at selected times, relative to initiation of deep convection, during the CA22SH15BZ60 simulation: (a) 2, (b) 10, (c) 18, and (d) 30 h. The top and right axes indicate longitude and latitude, respectively; the bottom and left axes indicate grid indices on the 30-km domain.

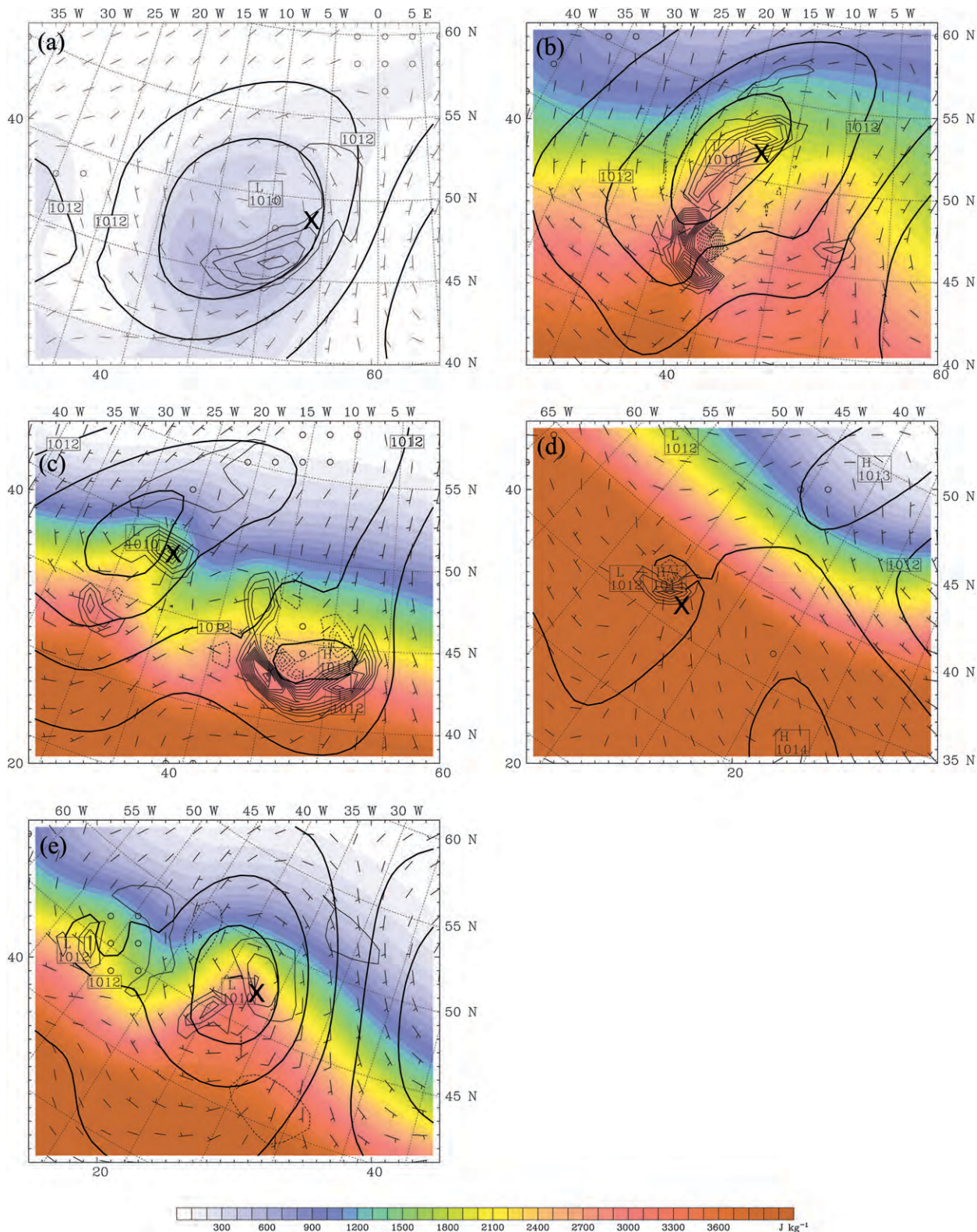
area of strong frontogenesis to the south of the surface pressure minimum is associated with an area of convection that does not develop an MCV.

Two separate MCSs developed in the coarse-resolution CA15SH30BZ60 simulation, so we conducted two separate finer-resolution simulations for this experiment. We designated these two simulations as CA15SH30BZ60-1 and CA15SH30BZ60-2. The first MCS (CA15SH30BZ60-1;

Fig. 4c) developed near the center of the baroclinic zone, and the second (CA15SH30BZ60-2; Fig. 4d) developed 20 h later and farther southwest.

In the CA15SH30BZ60-1 simulation (Fig. 4c), the strongest area of frontogenesis near 42°N, 10°W is at the southern end of an area of less organized, weaker convection associated with the initial perturbation vortex. This earlier convection weakened as the baroclinic

FIG. 4. CAPE (J kg^{-1} ; shading), surface pressure (hPa; thick black contour lines; contour interval 1 hPa), sum of the deformation and divergence terms of the Miller frontogenesis function [$\text{K (100 km h}^{-1})^{-1}$; thin black contour lines], and horizontal flow (wind barbs; full barb = 5 m s^{-1}) on the 90-km (outermost) grid immediately preceding initiation of deep convection for the following experiments: (a) CA00SH15BZ60; (b) CA22SH15BZ60; (c) CA15SH30BZ60-1; (d) CA15SH30BZ60-2; and (e) CA15SH30BZ30. The frontogenesis contours have the following properties in the individual panels [zero contour omitted; units of $\text{K (100 km h}^{-1})^{-1}$]: (a) low 0.01, high 0.04, interval 0.01; (b) low -0.08 , high 0.09, interval 0.01; (c) low 0.06, high 0.24, interval 0.02; (d) low -0.3 , high 0.5, interval 0.1; and (e) low -0.02 , high 0.03, interval 0.01. The "X" marks the location of the initiation of deep convection. The top and right axes indicate longitude and latitude, respectively; the bottom and left axes indicate grid indices on the 90-km domain.



cyclone developed farther west, near 30°W. The target MCS then initiated within this baroclinic cyclone, unassociated with the initial vortex. Such an outcome, on its own, provides strong evidence of the interdependency between the moist baroclinic cyclone and the MCS.

The CA15SH30BZ60–2 MCS (Fig. 4d) develops within the weakest cyclone of any of the experiments (in terms of surface pressure perturbation), but a distinct trough is still present. The weaker surface pressure minimum is partly due to the latitude (37°N) but may also be a reflection of its development south of the strongest baroclinic zone. The initiation here may be more CAPE-driven than cyclone-driven, but a moist baroclinic cyclone develops nonetheless.

In the experiment CA15SH30BZ30 (Fig. 4e), the baroclinic cyclone develops in association with the initial perturbation vortex. The MCS initiates in the same favored location slightly downshear from the surface pressure minimum in an area with strong meridional variation in CAPE.

In the CA22SH08BZ60 experiment (not shown), neither deep moist convection nor a strong surface low ever developed. The surface pressure minimum attained during the simulation was only 2 hPa deeper than the basic state. The shear of $0.75 \text{ m s}^{-1} \text{ km}^{-1}$ in this particular experiment was likely too weak to be considered baroclinically unstable since it is only one-fourth the value of the Eady-type basic state. Without any significant forcing for upward vertical motion due to synoptic-scale processes, no organized MCS ever developed.

In the following discussion, we estimate the strength of the MCV by taking the maximum difference in zonal winds between the northern side and the southern side of the cyclonic circulation in Fig. 5. The MCSs in all simulations (except for the experiment CA22SH08BZ60) evolve similarly, yet there are some noteworthy differences. Ten hours after initiation (Figs. 2c and 5), the simulations all feature an MCS with a cyclonic circulation (MCV) at 700 hPa, but the size of the MCS and strength of the circulation vary from case to case. In the CA00SH15BZ60 simulation (Fig. 5a), only weak CAPE (less than 700 J kg^{-1}) is available to the MCS, and consequently the size of the MCS and the strength of the circulation are much less than in the other conducted experiments. Despite the strength and width of the baroclinic zone being identical to that in the experiment CA22SH15BZ60 (see Fig. 2c), the MCS is much less extensive, and the circulation is much weaker.

In the CA15SH30BZ60–1 simulation (Fig. 5b), the MCS and MCV have stronger 700-hPa winds than in the CA00SH15BZ60 simulation (Fig. 5a). Because of moderate CAPE and a doubly strong baroclinic zone (see Table 1), the increased wind speed is expected. Com-

pared to the CA22SH15BZ60 simulation (Fig. 3c), however, the convection on the north side of the MCS is somewhat weaker, and the MCV is only equally as strong. Despite the stronger baroclinic zone relative to the CA22SH15BZ60 simulation, the lack of strength can be explained by two factors. First, there is less CAPE in the center of the baroclinic zone (see Table 1), and the CAPE diminishes to zero north of the baroclinic zone. Second, the vortex that was inserted into the initial state reduced the CAPE to the east of the developing MCS. The thermal and moisture advection by the north-to-south flow on the west side of the vortex was the primary cause of diminished CAPE. Additionally, the disorganized area of deep, moist convection that developed in association with the initial vortex consumed a small amount of CAPE.

The largest MCS in all the simulations was in the CA15SH30BZ60–2 experiment (Fig. 5c). Because it developed within an extensive area of large CAPE, convection was able to spread north and south of the developing MCV, and so the shape of the MCS most strongly resembles that of the CA22SH15BZ60 simulation. The strong 700-hPa rear inflow, reaching 37 m s^{-1} near 35.5°N 43.5°W, demonstrates the impact of a doubly strong baroclinic zone relative to the CA22SH15BZ60 simulation.

As in the CA15SH30BZ60–1 simulation, the effects of reduced CAPE to the north of the baroclinic zone (only 510 J kg^{-1} at 50°N compared to 1513 J kg^{-1} in the CA22SH15BZ60 simulation) are evident in the CA15SH30BZ30 simulation (Fig. 5d), where the convection on the northern side of the MCS is somewhat less extensive than in the CA22SH15BZ60 (Fig. 2c) and CA15SH30BZ60–2 (Fig. 5c) simulations. The CA15SH30BZ30 simulation (Fig. 5d) has the strongest vortex in Fig. 5 with a maximum difference in zonal winds (from the north side to the south side of the vortex) of approximately 45 m s^{-1} .

The MCS development within the large-scale baroclinic cyclone looks qualitatively very similar in all experiments: the deep moist convection is located within or around the deepening baroclinic cyclone, as already revealed in Fig. 3. The dynamically significant differences among the experiments are most easily revealed by plotting the time series of the surface pressure minimum (Fig. 6) relative to initiation time. The CA00SH15BZ60 cyclone experiences the least deepening of all the cases, which is not surprising given the modest shear and near-zero CAPE of the initial state. The experiment CA22SH15BZ60 has the same basic state shear, but its cyclone deepening is considerably faster. The only major difference between these two simulations is the initial CAPE, strongly indicating that the latent heat release within an MCS has a major effect on the larger-scale, baroclinic cyclone development.

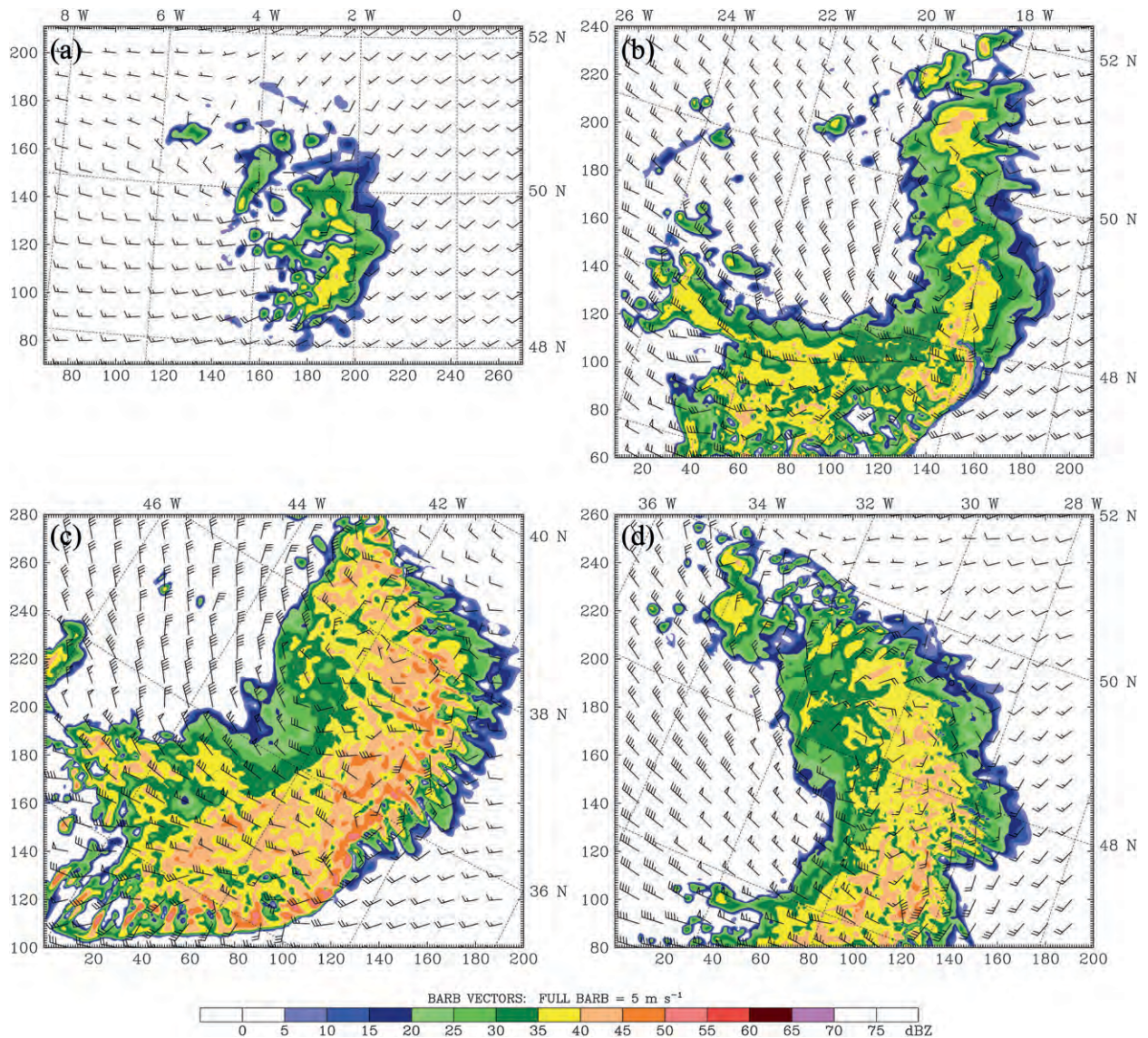


FIG. 5. Model-derived reflectivity (dBZ; shading) and horizontal flow (wind barbs; full barb = 5 m s^{-1}) at 700 hPa on the 3.3-km grid approximately 10 h after initiation of deep convection for the following experiments: (a) CA00SH15BZ60, (b) CA15SH30BZ60-1, (c) CA15SH30BZ60-2, and (d) CA15SH30BZ30. The top and right axes indicate longitude and latitude, respectively; the bottom and left axes indicate grid indices on the 3.3-km domain.

The CA15SH30BZ60-2 simulation deepens more slowly than all but the CA00SH15BZ60 experiment. The cold pool in this case is strongest (2-m temperature perturbation up to 18 K), thereby increasing the surface pressure. Additionally, the cyclone develops 10° south of the center of the initial baroclinic zone, which places it in a less favorable location with respect to the large-scale dynamics.

The remaining two cases experience a nearly equally rapid deepening that is consistent with what one might expect for cyclones developing near the center of the baroclinic zone in moderate shear. The deepening in the

CA15SH30BZ30 experiment slows about 25 h after initiation as the cyclone moves north of the baroclinic zone and occludes. In the CA15SH30BZ60-1 simulation, the baroclinic zone is wider. Thus, the cyclone can continue to extract energy from the basic state, and it continues to deepen.

b. Energy conversion as related to scale interaction

The results of the energy conversion calculations show dramatically different energy conversion in the CA22SH15BZ60 and CA00SH15BZ60 simulations (Fig. 7), which is consistent with the differences presented

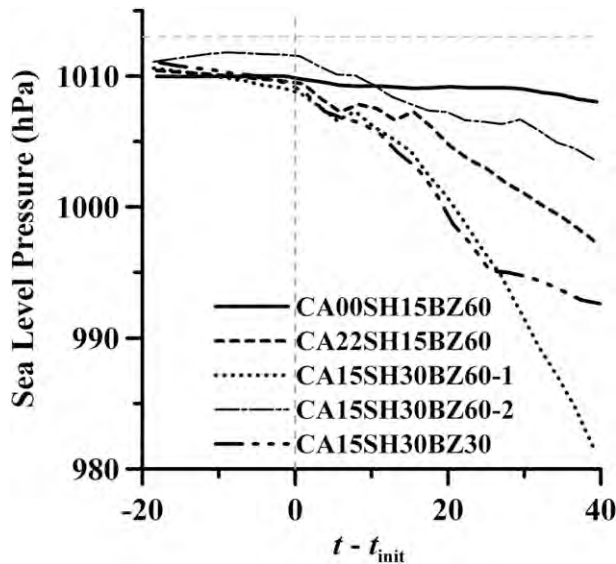


FIG. 6. Time series (h) of minimum surface pressure (hPa; taken from 90-km grid) relative to the time of initiation of deep convection (t_{init}) for the CA00SH15BZ60 (solid), CA22SH15BZ60 (dashed), CA15SH30BZ60-1 (dotted), CA15SH30BZ60-2 (dotted-dashed), and CA15SH30BZ30 (triple dotted-dashed) simulations.

in Fig. 6. The CA22SH15BZ60 simulation (Fig. 7a) has more than an order of magnitude greater diabatic production of APE (G_E) than the CA00SH15BZ60 run does (Fig. 7b). The evolution of G_E , as well as the conversion of basic-state APE to eddy APE (C_A) for the CA22SH15BZ60 simulation, shows some rather interesting characteristics. First, the diabatic term G_E undergoes a sudden increase as the convection develops,

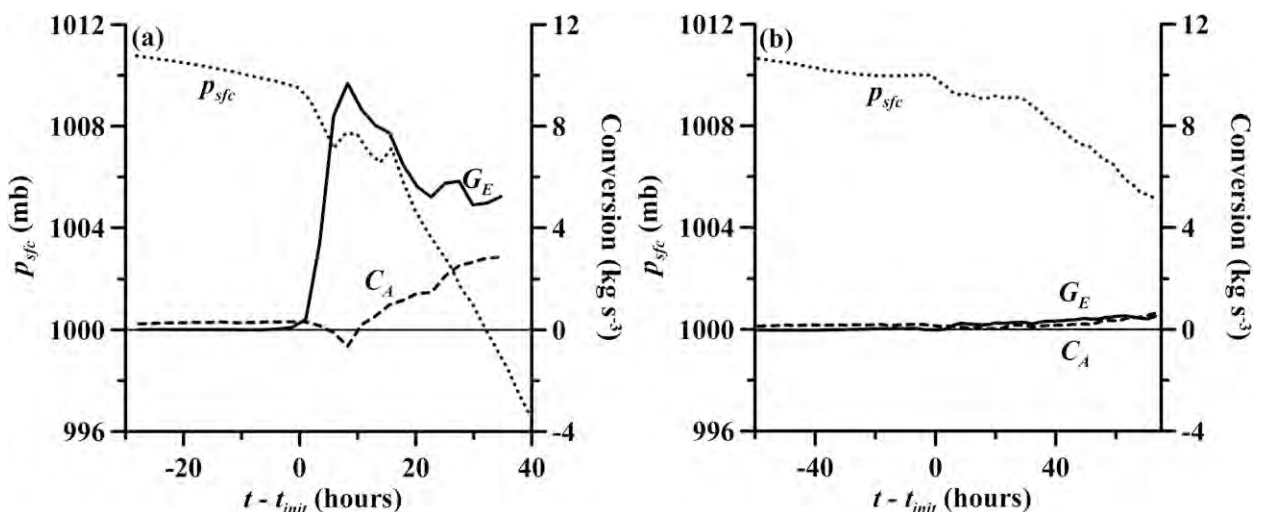


FIG. 7. Time series of the minimum surface pressure (hPa; dotted line), conversion of basic-state APE to eddy APE (C_A ; kg s^{-3} ; solid line), and conversion of diabatic heat energy to eddy APE (G_E ; kg s^{-3} ; dashed line), computed on the 90-km grid for an area with dimensions of 30° longitude \times 20° latitude centered on the surface pressure minimum for the (a) CA22SH15BZ60 and (b) CA00SH15BZ60 simulations.

but the baroclinic conversion C_A diminishes. We suspect that during this period some kinematic reorganization is occurring because as the MCS develops, its cold pool spreads throughout a portion of the warm sector east of the surface low, interfering with the baroclinic conversion process of the large-scale system (see Fig. 3). Meanwhile, as will be seen in section 3e, the MCV undergoes rapid intensification (between 950 and 450 hPa), and discernable cyclonic rotation develops at the MCV scale (Figs. 2a–c). Thereafter, the baroclinic conversion term C_A increases again and becomes dramatically larger than in the CA00SH15BZ60 simulation (Fig. 7b). Rapid deepening of the surface low resumes 16 h after initiation.

In both experiments, once convection develops and the larger-scale system undergoes a few hours of adjustment, overall system-scale deepening (which can be considered a combination of the MCV scale and the synoptic-scale deepening) occurs much more quickly. The deepening is far greater for the CA22SH15BZ60 experiment than in the CA00SH15BZ60 simulation.

As has been discussed in sections 3a and 3b and in C1, the MCS development depends on the larger, moist baroclinic cyclone, which provides the deep, persistent lift and low-level inflow of moisture to initiate the convection. The results of the energy conversion calculations here—particularly with the more rapid deepening in the CA22SH15BZ60 experiment relative to the CA00SH15BZ60 experiment—suggest that the relationship also acts conversely. That is, the MCV has a feedback on the developing baroclinic system, causing it to deepen more quickly than it would in the absence of the strong diabatic heating.

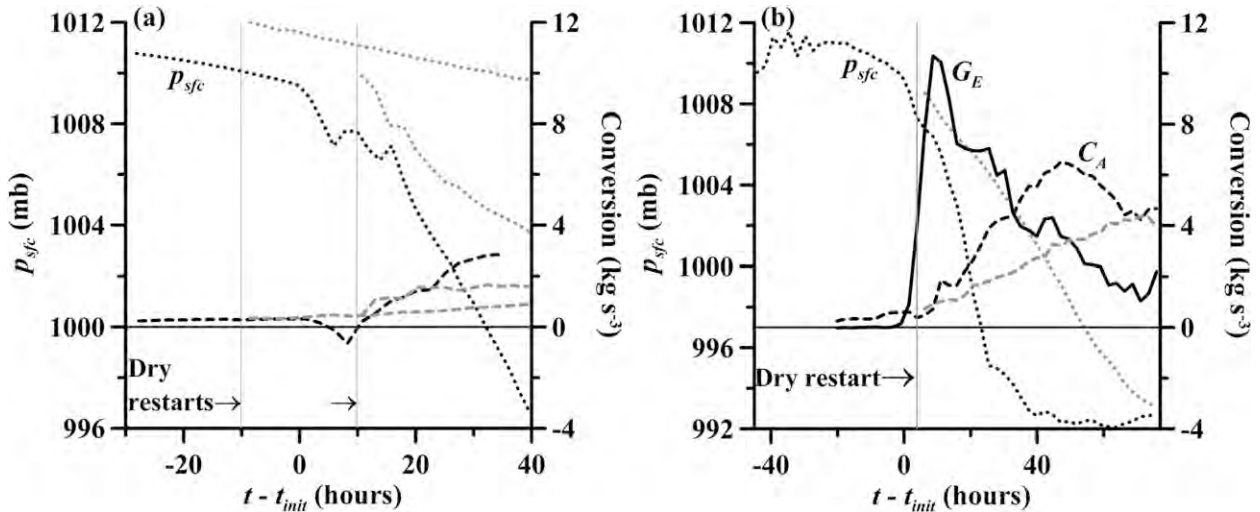


FIG. 8. Energy conversion comparison between moist simulations (black lines) and simulations with latent heating shut off (gray lines) for the (a) CA22SH15BZ60 and (b) CA15SH30BZ30 experiments. For notation, see Fig. 7.

c. Dry simulations

Despite the initial decrease of baroclinic conversion C_A as the MCS develops, the net effect of the diabatic heating on C_A is positive. The results of all three dry restarts (see Table 3) show that the baroclinic conversion C_A is less whenever the diabatic heating is removed from the simulation (Fig. 8). In the CA22SH15BZ60 restarts (Fig. 8a), the magnitude of C_A depends on the time the restart is made. If the restart is performed 10 h before initiation, C_A reaches only one-third its corresponding value in the moist simulation. If the restart is performed 10 h after initiation, C_A remains nearly as large as in the moist case until approximately $t - t_{\text{init}} = 20$ h. Thereafter, it remains approximately constant while C_A of the corresponding moist experiment continues to increase. In both dry restarts, the deepening of the surface low is less rapid than in the moist simulation, and in neither dry case does the deepening rate appear exponential. The lack of apparent exponential deepening in the dry restarts does not necessarily indicate baroclinic stability. Rather, it may be due to the fact that the “dry” e -folding time scale is long compared to the “moist” e -folding time scale, making it difficult, within the time scales examined here, to extract the unequivocal dry exponential growth rate.

In the CA15SH30BZ30 dry restart (Fig. 8b), the baroclinic conversion term C_A increases about half as fast as it does in the corresponding moist experiment. In the moist case, C_A reaches its peak 47 h after initiation and then begins to decrease as the system moves north of its baroclinic support and occludes. In the dry case, the conversion of mean-state APE to eddy APE is slower, so the occlusion process is delayed and the system con-

tinues deepening, although not as fast as in the moist case. By $t - t_{\text{init}} = 76$ h, C_A in the dry case has caught up to its value in the moist case, and the surface low is about as deep. Given these results, there may be enough baroclinic instability in this case for the rapid deepening to occur without convection. It is nonetheless evident that the convection significantly accelerates the intensification process.

The results of all restarts suggest that the MCS has a projection onto a packet of unstable moist baroclinic modes and promotes baroclinic development. From a qualitative point of view, the overall length of the large-scale wave changes little during the simulation (see Fig. 3), which suggests a preferred wavenumber near the most rapidly growing moist baroclinic mode (MM04). During the first 10 h after initiation in the CA22SH15BZ60 experiment, the MCV intensifies on its own scale (essentially, the scale of the convective system), but later, once reorganization of the system occurs, deepening proceeds on the larger scales as well. These same results are seen in the CA15SH30BZ30 experiment. Our overall results lend support to the findings of Galarneau et al. (2009), who likewise documented the upscale growth of an MCV and its subsequent interaction with a baroclinic zone from 10 to 14 June 2003, during BAMEX. Their analysis demonstrated the influence of MCV dynamics on guiding the organization of a larger-scale baroclinic wave.

d. PV structure

The initial PV production is quite strong, localized, and associated with the initial convective elements (Figs. 2a,c and 9a,b). Thereafter, as the cold pool grows and

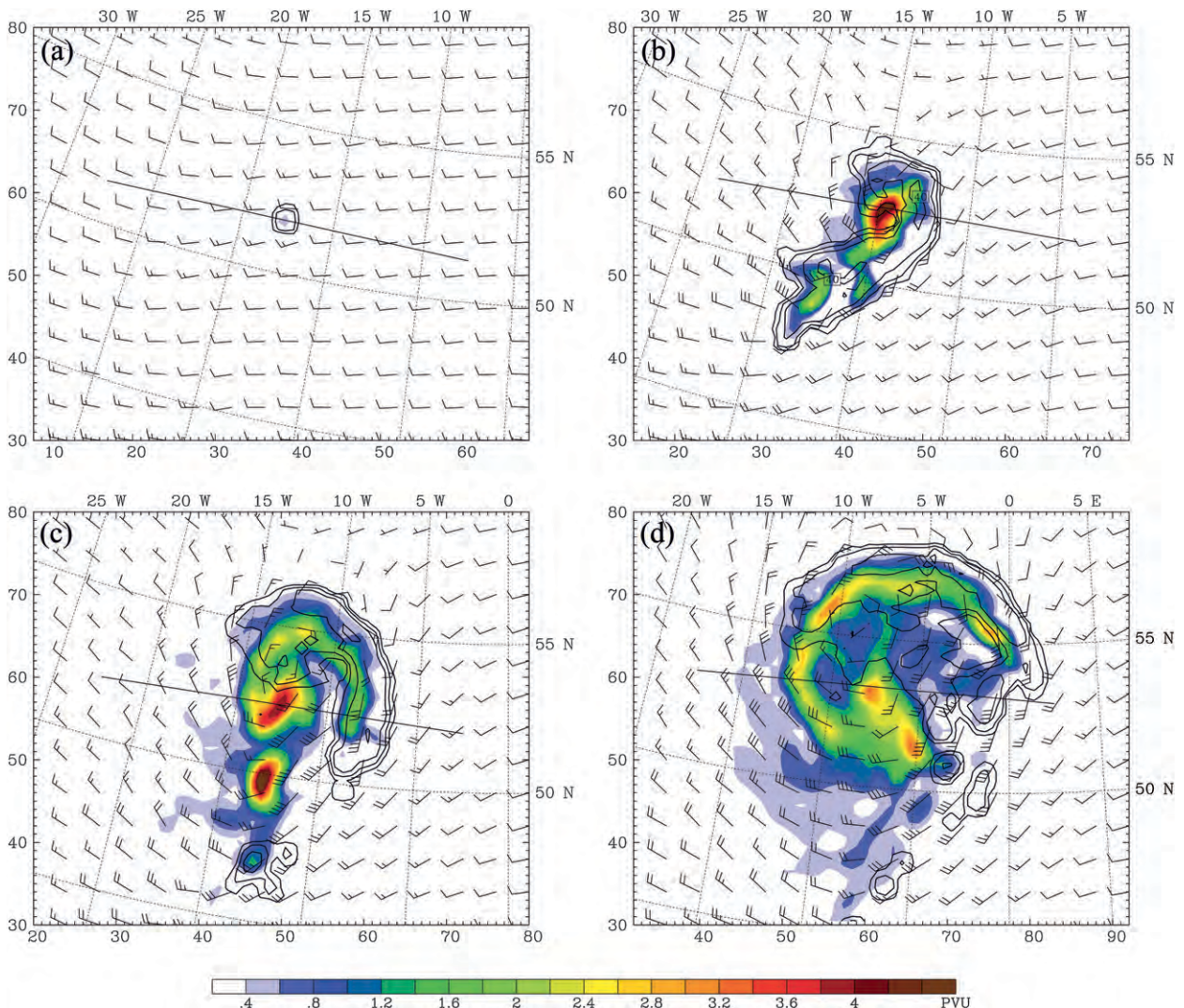


FIG. 9. Potential vorticity (PVU; shading), model-derived reflectivity (dBZ; black contour lines; contour interval of 10 dBZ from 10 to 40 dBZ), and horizontal flow (wind bars; full barb = 5 m s^{-1}) at 700 hPa on the 30-km grid for the CA22SH15BZ60 experiment at the following times relative to the initiation of deep convection: (a) 2, (b) 10, (c) 18, and (d) 30 h. The top and right axes indicate longitude and latitude, respectively; the bottom and left axes indicate grid indices on the 30-km domain. The straight lines in the figure panels indicate the positions of the vertical cross sections appearing in Fig. 10.

the convection moves radially outward from the MCV (Figs. 9c,d), the strongest PV production moves outward as well. Viewed on the 3.3-km grid (Conzemius and Montgomery 2009), the leading line of convection produces strong couplets of positive and negative PV, with magnitudes reaching 30 PV units. These centers fill, merge, and are advected rearward from the convection into the stratiform region, closer to the MCV center, where PV production continues. Davis and Galarnau (2009) documented a similar process for two BAMEX MCVs. On the coarser 30-km grid (Fig. 9), the process results in a strong, positive PV anomaly appearing behind the leading convective line. Upscale growth of the entire system occurs as

the PV associated with the continuing convection becomes cyclonically wrapped around the original positive PV perturbation. Although this line of newly created PV wraps back into the center of circulation (because of differential advection), once it is formed there is little or no shearing or filamentation of this new PV that would indicate a Rossby wave “spinup” process (Carr and Williams 1989; Montgomery and Kallenbach 1997).

Figure 10 shows the PV vertical cross sections corresponding to the lines shown in Fig. 9. The cross sections reveal the typical MCV structure, with strong positive PV anomalies throughout the troposphere and negative anomalies found downshear in the upper troposphere

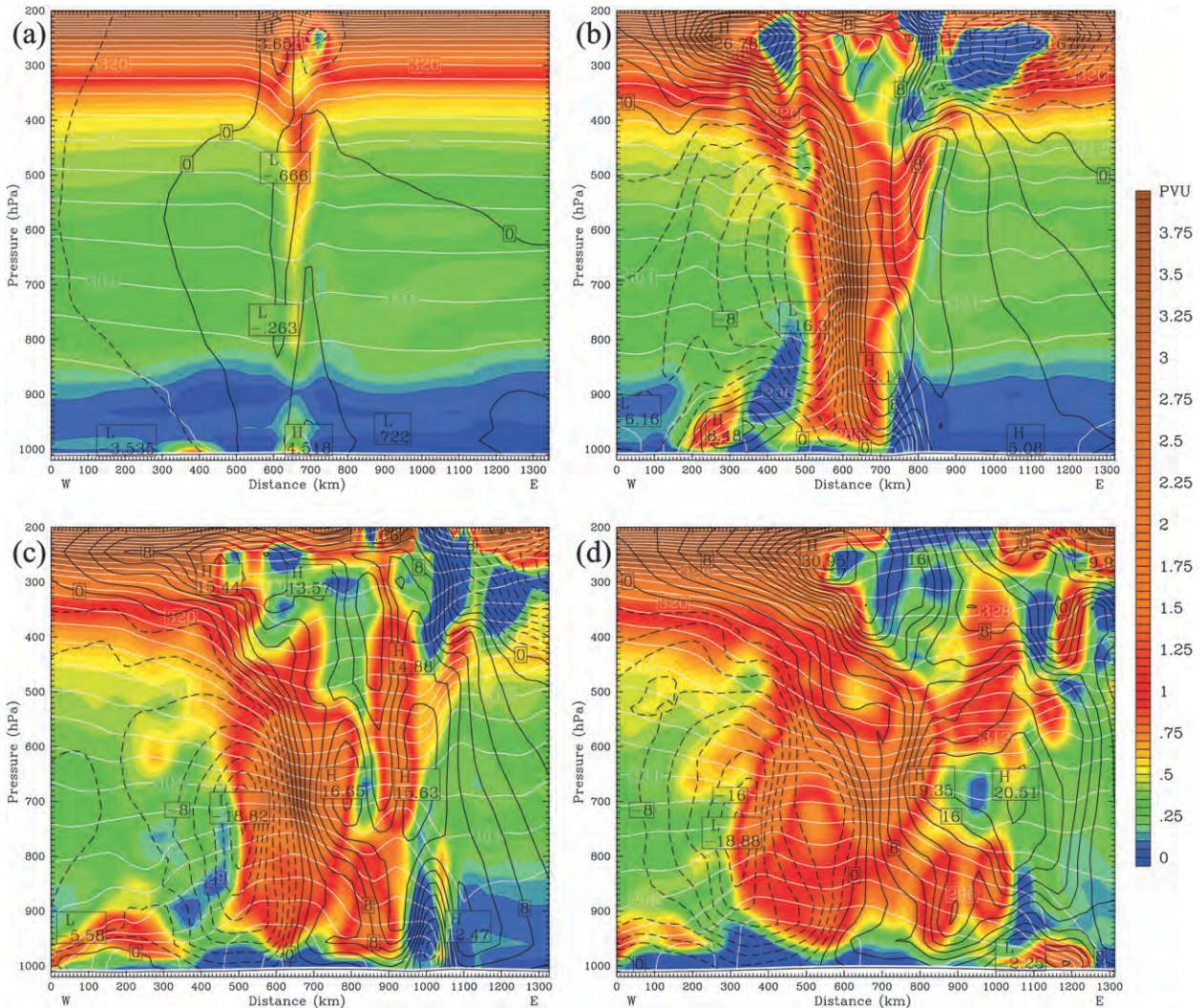


FIG. 10. Potential vorticity (PVU, $10^{-6} \text{ m}^2 \text{ s}^{-1} \text{ K kg}^{-1}$; shading), potential temperature (white lines; contour interval 2 K), and meridional wind (black lines; contour interval 2 m s^{-1}) on the 30-km grid in the CA22SH15BZ60 simulation for the following cross sections and times relative to the initiation of deep convection: (a) 2 h from 51.4°N , 27.5°W to 51.4°N , 7.5°W ; (b) 10 h from 52.2°N , 24°W to 52.2°N , 4°W ; (c) 18 h from 52°N , 22.5°W to 52°N , 2.5°W ; and (d) 30 h from 53°N , 17.5°W to 53°N , 2.5°E . See Fig. 9 for the horizontal axes of these cross sections.

and stratosphere. The vortex at 700 hPa rapidly intensifies during the first 10 h after initiation (Figs. 10a,b) and then grows upscale while more slowly increasing in intensity (Figs. 10c,d). Such an evolution of vertical PV structure is consistent with the outward movement of the diabatic PV production associated with the leading convection. At later stages in the development of the mesoscale vortex (Figs. 10c,d), most of the increase in meridional winds is associated with the amplification of the large-scale baroclinic wave. By 30 h after initiation (see Fig. 10d), the diameter of the vortex, defined in terms of maximum meridional wind, is approximately 750 km, which is somewhat more consistent with the size of a typical baroclinic wave than that of an MCV (Davis

and Trier 2007). The MCV in this experiment undergoes significant upscale growth as the convection is continually adding to the PV within the entire system. Such upscale growth has also been observed in situations when repeated convection, occurring over several days, allows for reintensification of the MCV (Fritsch et al. 1994; Galarneau et al. 2009).

In summary, as the MCS grows in size and the leading convective elements advance outward (Fig. 9), the PV production expands outward as well, and the whole PV anomaly undergoes an upscale growth. In fact, by the end of the simulation, it becomes difficult to clearly distinguish the MCV from the deepening baroclinic system as if the two were involved in a seamless transition.

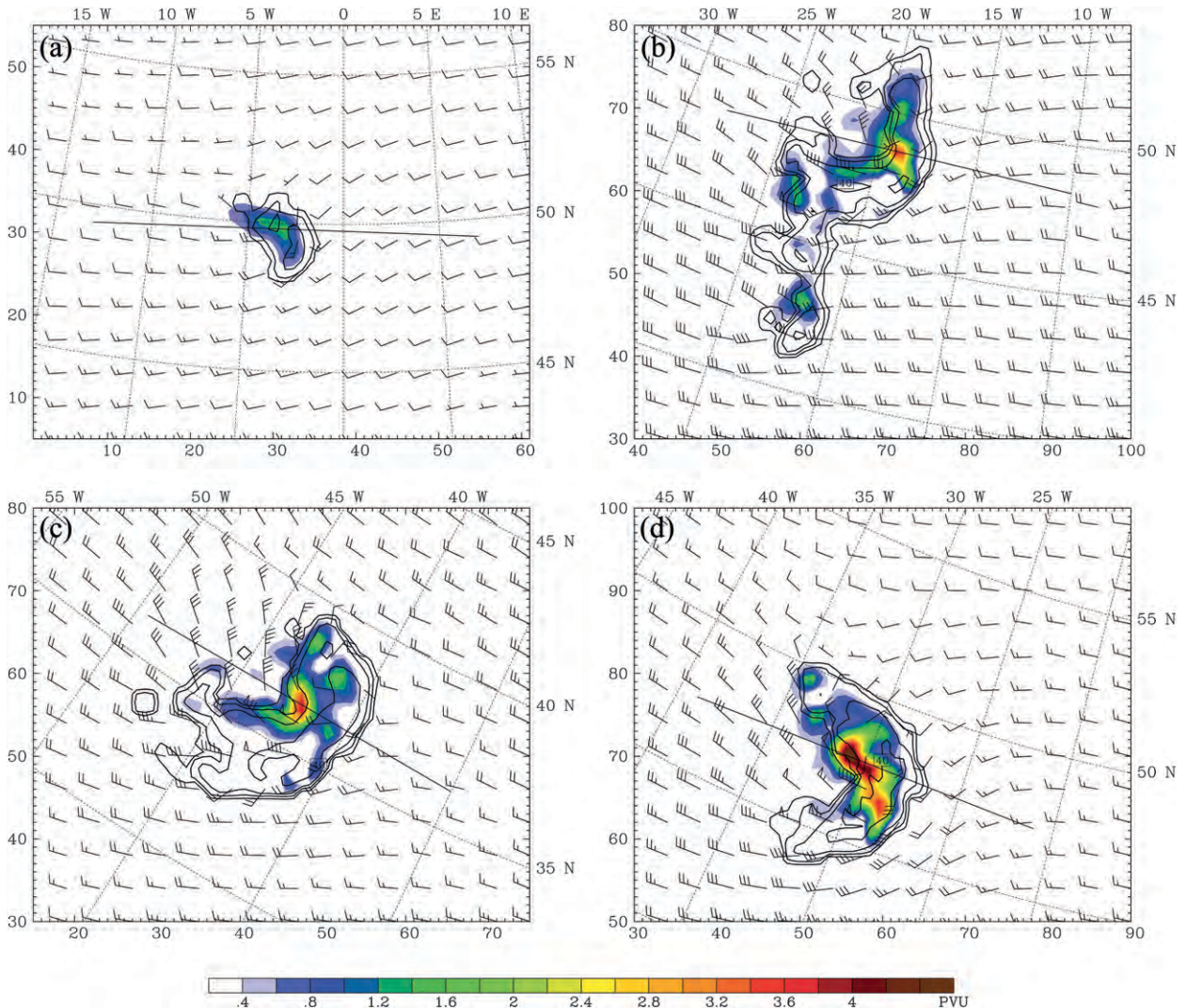


FIG. 11. Potential vorticity (PVU; shading), temperature (K; black contour lines) and horizontal flow (wind barbs; full barb equals 5 m s^{-1}) at 700 hPa on the 30-km grid for the following experiments approximately 10 h after the initiation of deep convection: (a) CA00SH15BZ60; (b) CA15SH30BZ60-1; (c) CA15SH30BZ60-2; and (d) CA15SH30BZ30. The top and right axes indicate longitude and latitude, respectively; the bottom and left axes indicate grid indices on the 30-km domain. The straight lines in the figure panels indicate the positions of the vertical cross sections appearing in Fig. 12.

Intense PV production occurs at the mesoscale (along the main squall line) and becomes entrained into the synoptic-scale PV anomaly. This is similar to the process Trier et al. (1997) have found for the entrainment of PV into mesoscale line-end vortices.

Essentially all the idealized cases experience this characteristic evolution. By 10 h after initiation (Figs. 11 and 12), all feature a positive PV anomaly immediately behind the line of heaviest reflectivity, and all have the same characteristic PV vertical structure (C1; Fritsch et al. 1994; Raymond and Jiang 1990).

Despite these commonalities, a few dynamically important differences arise among the experiments. The

CA00SH15BZ60 run (Figs. 11a and 12a), with its relatively small CAPE and therefore small latent heat content, has the least diabatic PV production. Its MCV is the weakest among all the cases, reaching roughly 5 m s^{-1} tangential velocity (we take the maximum tangential velocity as the average absolute value of maximum and minimum meridional winds). The MCV is also sufficiently sheared that its tilt becomes visible at these scales (note that the aspect ratio of these plots does not easily reveal tilt). The CA00SH15BZ60 experiment also has the lowest height of maximum tangential winds (which we identify by the average height of the minimum and maximum meridional wind component) at about 840 hPa.

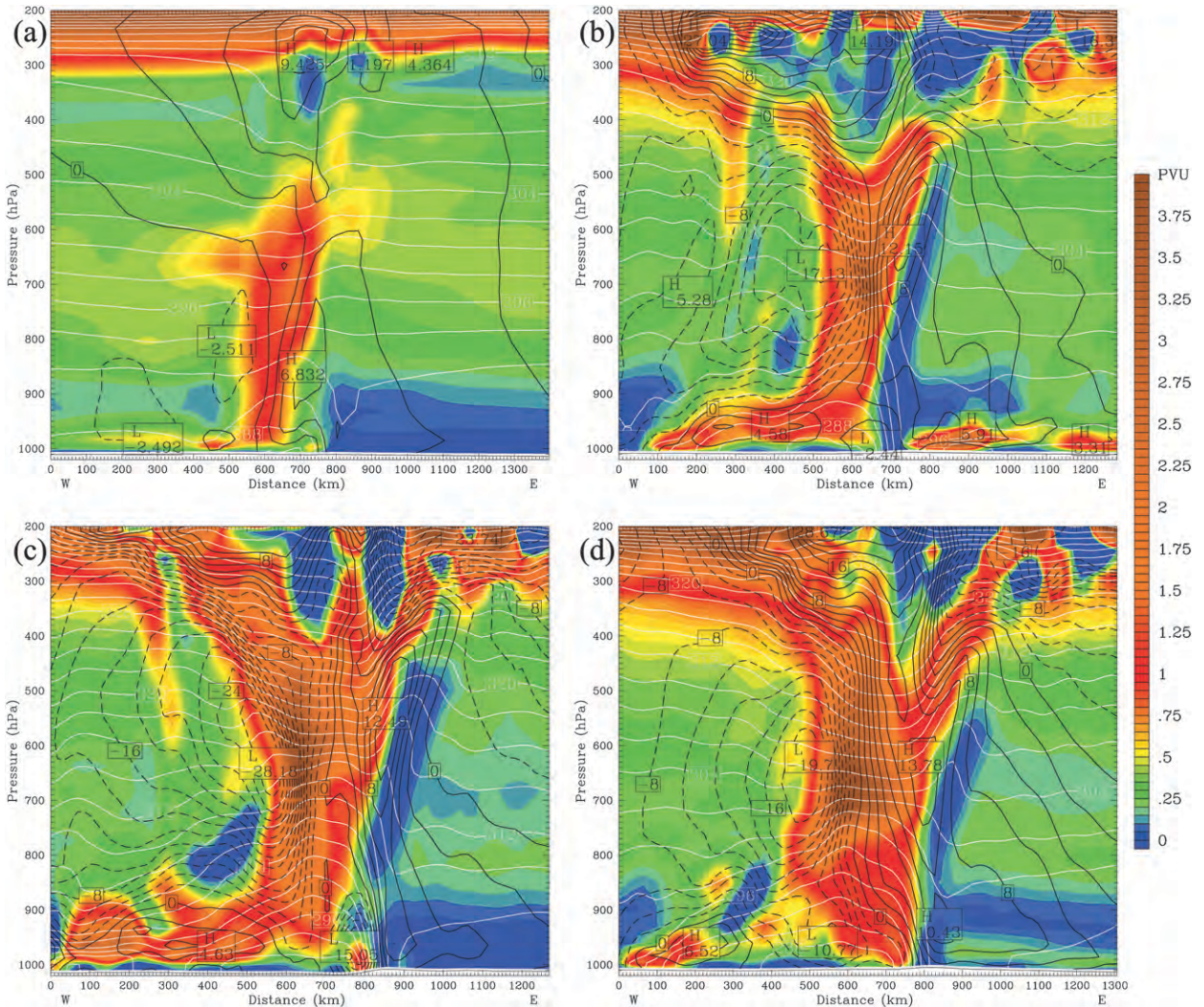


FIG. 12. Vertical cross section of the potential vorticity (PVU, or $10^{-6} \text{ m}^2 \text{ s}^{-1} \text{ K kg}^{-1}$; shading), potential temperature (white contour lines; interval 2 K), and meridional velocity (black lines; contour interval 2 m s^{-1} ; dashed lines for negative contours) approximately 10 h after the initiation of deep convection for (a) CA00SH15BZ60 run along a cross section from 49.4°N , 13°W to 49.4°N , 7°E ; (b) CA15SH30BZ60-1 from 48.4°N , 28°W to 48.4°N , 10°W ; (c) CA15SH30BZ60-2 from 36.3°N , 49.5°W to 36.3°N , 35°W ; and (d) CA15SH30BZ30 from 47.4°N , 39°W to 47.4°N , 21°W . See Fig. 11 for the horizontal axes of these cross sections.

In the CA22SH15BZ60 simulation (Figs. 9b and 10b), the MCV is much stronger and is somewhat taller than in the CA00SH15BZ60 simulation. It develops a stronger cold pool, and its maximum tangential winds (14 m s^{-1}) occur near 800 hPa, higher than in the CA00SH15BZ60 run.

The greater APE in the basic state of the CA15SH30BZ60 experiment appears to have a strengthening effect on the MCVs. The vortices in both CA15SH30BZ60 simulations are as strong as or stronger than that in the CA22SH15BZ60 simulation. Despite access to less CAPE, the MCV in the CA15SH30BZ60-1 simulation (Figs. 11b and 12b) has tangential winds of 15 m s^{-1} . The CA15SH30BZ60-2 MCV (Figs. 11c and

12c), with its access to undiminished CAPE and significant shear, has tangential winds with values up to 20 m s^{-1} . The CA15SH30BZ60-2 vortex also has the highest altitude of maximum tangential winds. Because the CA15SH30BZ60-2 MCV is at the lowest latitude of all the experiments (36.5°N), the thermal vertical structure of the basic state (higher tropopause height, larger CAPE) allows for much more vigorous convection, and the maximum heating rate occurs at a higher altitude. This point will be further elucidated in section 3e.

The CA15SH30BZ30 simulation (Figs. 11d and 12d) has at least as strong a vortex as in the two CA15SH30BZ60 simulations. The shear and CAPE in the background state are the same as in the

CA15SH30BZ60 experiments, but the baroclinic zone is only half as wide, resulting in greater cyclonic relative vorticity on the poleward side of the baroclinic zone where the MCV develops.

e. Further comparison with BAMEX observations

An initial comparison with BAMEX observations was made in C1. Davis and Galarneau (2009) have made more detailed comparisons between simulations and observations for two BAMEX IOPs. Our intent here is to perform a cursory investigation into the similarities and differences between the simulated MCVs in the present study and the observed MCVs in BAMEX. We will identify the likely causes of any differences.

The two most important differences between the simulations and the BAMEX IOPs were that (i) the simulations were performed in an environment with relatively little initial baroclinic wave amplitude (our initial condition is a sum of surface edge waves in the Eady model) compared to typical atmospheric cases and, therefore, nearly pristine mean-state APE; and (ii) except for the CA00SH15BZ60 experiment, the initial state had untapped areas of CAPE in the center of the baroclinic zone and everywhere equatorward. Because of the extensive areas of CAPE and largely untapped APE in the initial state, the simulated MCSs can expand to cover exceptionally large areas, and their MCVs, with ever-present convection, continually grow in size to the full cyclone wave scale over the course of the simulation, as both CAPE and basic state APE are consumed. In actual atmospheric cases, convective activity is intermittent, thus frustrating the upscale growth of the MCV or allowing the MCV to be destroyed by the background shear (C1; MM05; Fritsch et al. 1994).

The comparisons with BAMEX IOPs are probably best made about 8 to 16 h after convective initiation in the idealized simulations, when the MCVs are relatively young. After that point, the continued expansion of the convective systems and deepening of the baroclinic waves, although not entirely unrealistic, seem less typical of summerlike conditions. Table 4 shows the comparisons.

One particular case of interest was IOP 8. Its MCV was the strongest observed in BAMEX, yet the shear over its depth was the weakest. In an attempt to simulate an MCV in similar conditions, we created the CA22SH08BZ60 experiment, but organized convection never developed in that simulation. Upper-air analyses for IOP 8 (Davis and Trier 2007; Davis and Galarneau 2009) actually showed the target MCV to be on the cyclonic shear side of a band of roughly 20 m s^{-1} mid-tropospheric flow. The area just south of the MCV had larger vertical shear in a narrow baroclinic zone, which is more typical of warm season conditions than the wider

baroclinic zones of the idealized simulations in the present study.

For all simulated MCVs in Table 4, the vertical shear is larger than in IOP 8. Some insight into the reasons for this can be gained by plotting the time series of shear (see section 2f) for the CA22SH15BZ60 and CA15SH30BZ30 simulations (Fig. 13). Although the basic state shear was weaker in the CA22SH15BZ60 experiment (Fig. 13a), the shear increased during the simulation (Fig. 13a). A closer look at the 8-km winds and PV structure in the CA22SH15BZ60 simulation (not shown) revealed that the upper tropospheric negative PV anomaly was displaced downshear from the midtropospheric PV positive anomaly. This displacement resulted in increased southwesterly flow directly above the low-level vortex at $z = 1 \text{ km}$. In essence, the shear remained strong because the MCV remained in the baroclinic region throughout its lifetime.

In the CA15SH30BZ30 experiment (Fig. 13b), the narrower baroclinic zone allowed the growing MCV to move north into a region with less shear. Although (for the sake of consistency in our analysis) the shear values reported in Table 4 are significantly larger than the values in BAMEX IOP 8, the shear in the simulated MCV eventually decreased to values consistent with IOP 8. By that time, however, the system scale was much larger than the MCV reported in IOP 8. In all other simulations, the broad baroclinic zone did not allow the MCV to move out of the region of deep layer shear, so the reported values changed less than in the CA15SH30BZ30 experiment.

In general, the shear in the simulations covers the low to middle range of the BAMEX IOPs. Further simulations with relatively more intense baroclinic zones could be conducted to explore the upper range of BAMEX shear. Because the baroclinic zone in the CA15SH30BZ30 experiment was still somewhat wider than that prior to IOP 8, further simulations could also employ yet narrower initial baroclinic zones, but it is already clear from the present simulations that if the MCV is able to move out of the region of strong shear, it is more likely to acquire characteristics similar to the IOP 8 MCV.

Overall, the strength of the MCVs produced in the simulations is in rather good agreement with the intensity of the MCVs observed in BAMEX. The very small CAPE of the CA00SH15BZ60 experiment results in a weaker MCV, but the rest of the experiments develop MCVs that are roughly as intense as the observed MCVs (as measured by V_m), with tangential winds generally within the range of that observed in BAMEX. The CA15SH30BZ60-2 MCV was a bit stronger at 20 m s^{-1} , but its CAPE also lies outside the range observed in BAMEX. About 8–12 h after their development, the radii of maximum winds in all the simulated

TABLE 4. Properties of the simulated MCVs and MCVs observed in BAMEX; V_m is the maximum tangential velocity, R_m is the radius of maximum tangential velocity, and P_m is the pressure level of maximum tangential velocity.

Simulation or IOP	Date (2003)	V_m (m s ⁻¹)	R_m (km)*	P_m (hPa)	CAPE (J kg ⁻¹)**	Shear, 1–4 km (m s ⁻¹)	Shear, 1–8 km (m s ⁻¹)
CA00SH15BZ60	—	5	100 ↑	850	300	5	12
CA22SH15BZ60	—	14	100 ↑	800	2200	4	13
CA15SH30BZ60–1	—	15	100 ↑	650	1700	9	16
CA15SH30BZ60–2	—	20	150 ↑	580	4000	10	14
CA15SH30BZ30	—	17	150 ↑	630	2800	10	18
1	24 May	13	100	480	1000	12	14
4	2 Jun	15	150	650	1000	14	27
5	5 Jun	12	100	660	2000	12	32
8	11 Jun	15	150	660	2000	2	5
15	29 Jun	10	100	540	1700	8	13

* The up arrow in the R_m column is an indicator that R_m is increasing with time.

** CAPE in the BAMEX IOPs has been calculated from the Eta model analysis of CAPE at the point where the MCS was first defined. In the simulations, the CAPE value is taken from the location of deep convection initiation.

vortices fall within the range observed in the IOPs. This result provides strong indication that the structures being simulated herein are useful analogs of the observed MCVs. As already noted, however, because of the experimental setup the vortices in the idealized simulations continue to grow in size after the period of comparison.

One other final point of comparison is the altitude of maximum tangential winds. In BAMEX, the range presented is at a somewhat higher altitude (lower pressure) than in the simulations. In the simulations, the altitude of maximum tangential winds appeared to be related to latitude and CAPE, both of which also have an impact on the level of maximum diabatic heating. The initial-state thermal profiles at lower latitudes are more conducive to a heating maximum at a higher level. The equation for the material rate of change of PV (Holton 2004) implies cyclonic vorticity production below

the level of maximum heating (the PV production to which we refer is for parcels in a Lagrangian setting). By the invertibility principle, in the approximately moist neutral conditions within the MCS, most of the cyclonic PV anomaly will be manifest as a cyclonic wind anomaly. Thus, as the level of maximum heating is raised, the level of maximum tangential wind will also rise.

Indeed, the CA15SH30BZ60–2 experiment has the highest level of maximum tangential winds. All other simulated MCVs occurred north of 45°N where the tropopause height and CAPE were lower. The BAMEX MCVs were all observed south of 45°N.

4. Summary and conclusions

The summary and conclusions of this paper can be stated in terms of the initial goals set forth in section 1.

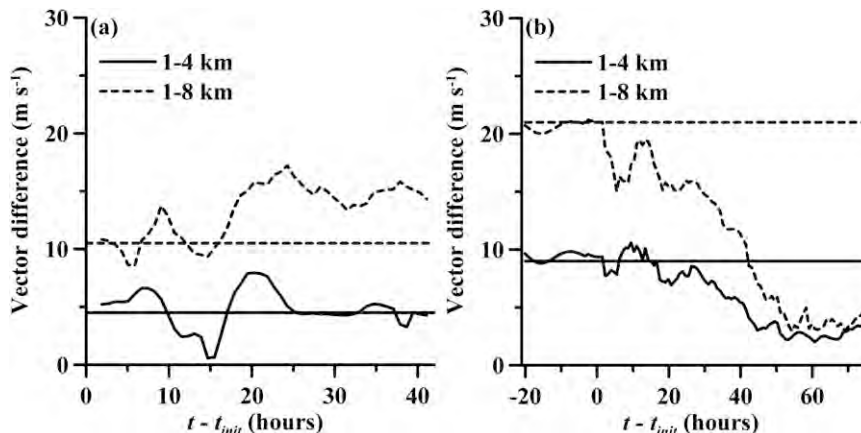


FIG. 13. Time dependence of the vector difference in horizontal velocity between 1 and 4 km MSL (solid lines) and between 1 and 8 km MSL (dashed lines) for the (a) CA22SH15BZ60 and (b) CA15SH30BZ30 simulations. The time-dependent plots are taken from the simulations, and the time-constant lines represent the shear in the background state.

- 1) The conducted simulations reveal an important synergistic (two-way) interaction taking place between the mesoscale (MCS–MCV) development and the synoptic-scale baroclinic waves. The results lend strong support to the hypothesis that the MCS and subsequent MCV development are dependent on the moisture flux and lift provided by a larger-scale system. In the simulations, the large-scale system was a growing baroclinic wave, but in the warm season atmosphere, it is quite plausible that more stationary large-scale structures such as the low-level jet on the North American plains may also play a role in providing this moisture flux, where such structures intersect baroclinic regions. In the opposite sense, the growth rate of the synoptic-scale system is enhanced by the diabatic production of PV and eddy available potential energy (APE) provided by the MCS. Together, these findings point to a synergistic interaction between the MCV and the larger synoptic-scale flow.
- 2) The spiral-shaped PV structures appearing in the x – y cross sections of the simulations are caused by intense PV production occurring in and just behind the leading convective line (at the edge of the cold pool) that advances outward from the MCV center. These new areas of PV then rotate cyclonically around the original center and gradually become entrained into, and more axisymmetric with, the main PV center as the whole system grows upscale.
- 3) Comparisons with the MCVs observed in the Bow Echo and Mesoscale Convective Vortex Experiment (BAMEX) show that the latitudinally broad baroclinic zones in the constructed basic states limited the variability of vertical shear experienced by the simulated MCVs relative to the MCVs of BAMEX. Also, the deepening of the surface lows is enhanced relative to what might be expected in warm season conditions. This is the result of the pristine initial state, in which baroclinic wave amplitude was initially very small. The basic state exhibited instability to moist baroclinic waves, and very large areas of CAPE were available to the first system that developed in the simulation. Nevertheless, the structures that developed had features similar to those observed in BAMEX, with the radii of maximum winds and the values of tangential winds being within the range observed in BAMEX.

In the light of making further comparisons with BAMEX MCVs, additional realism may be provided in future simulations by allowing for narrower baroclinic zones than have been simulated in the present study. This would permit MCVs to move in and out of regions

of deep layer shear and thereby allow us to explore the effects of changing shear on MCV dynamics. Finally, the sensitivity of the MCV dynamics to the diurnal cycle has not been actively explored in these simulations. These complex and physically relevant issues await further investigation.

Acknowledgments. This work was supported by NSF Grant ATM-0305412. We also thank Dr. Christopher Davis of NCAR for providing helpful comments. Additionally, we extend our thanks to Dr. Stanley Trier of NCAR and two anonymous reviewers for their help in improving this manuscript.

REFERENCES

- Bartels, D. L., and R. A. Maddox, 1991: Midlevel cyclonic vortices generated by mesoscale convective systems. *Mon. Wea. Rev.*, **119**, 104–118.
- Bluestein, H. B., 1992: *Observations and Theory of Weather Systems*. Vol. II, *Synoptic–Dynamic Meteorology in Midlatitudes*, Oxford University Press, 608 pp.
- Bryan, G. H., J. C. Wyngaard, and J. M. Fritsch, 2003: Resolution requirements for the simulation of deep moist convection. *Mon. Wea. Rev.*, **131**, 2394–2416.
- Carr, L. E., III, and R. T. Williams, 1989: Barotropic vortex stability to perturbations from axisymmetry. *J. Atmos. Sci.*, **46**, 3177–3191.
- Conzemius, R. J., and M. T. Montgomery, 2009: Clarification on the generation of absolute and potential vorticity in mesoscale convective vortices. *Atmos. Chem. Phys.*, **9**, 7591–7605.
- , R. W. Moore, M. T. Montgomery, and C. A. Davis, 2007: Mesoscale convective vortex formation in a weakly sheared moist neutral environment. *J. Atmos. Sci.*, **64**, 1443–1466.
- Cotton, W. R., and R. A. Anthes, 1989: *Storm and Cloud Dynamics*. Academic Press, 881 pp.
- Davis, C. A., and M. L. Weisman, 1994: Balanced dynamics of mesoscale vortices produced in simulated convective systems. *J. Atmos. Sci.*, **51**, 2005–2030.
- , and S. B. Trier, 2007: Mesoscale convective vortices observed during BAMEX. Part I: Kinematic and thermodynamic structure. *Mon. Wea. Rev.*, **135**, 2029–2049.
- , and T. J. Galarneau Jr., 2009: The vertical structure of mesoscale convective vortices. *J. Atmos. Sci.*, **66**, 686–704.
- , M. T. Stoelinga, and Y.-H. Kuo, 1993: The integrated effect of condensation in numerical simulations of extratropical cyclogenesis. *Mon. Wea. Rev.*, **121**, 2309–2330.
- , D. A. Ahijevych, and S. B. Trier, 2002: Detection and prediction of warm season midtropospheric vortices by the rapid update cycle. *Mon. Wea. Rev.*, **130**, 24–42.
- , and Coauthors, 2004: The bow echo and MCV experiment: Observations and opportunities. *Bull. Amer. Meteor. Soc.*, **85**, 1075–1093.
- Dunkerton, T. J., M. T. Montgomery, and Z. Wang, 2008: Tropical cyclogenesis in a tropical wave critical layer: Easterly waves. *Atmos. Chem. Phys. Discuss.*, **8**, 11 149–11 292.
- Fovell, R. G., and Y. Ogura, 1988: Numerical simulation of a mid-latitude squall line in two dimensions. *J. Atmos. Sci.*, **45**, 3846–3879.
- Fritsch, J. M., J. D. Murphy, and J. S. Kain, 1994: Warm core vortex amplification over land. *J. Atmos. Sci.*, **51**, 1780–1807.

- Galarneau, T. J., Jr., L. F. Bosart, C. A. Davis, and R. McTaggart-Cowan, 2009: Baroclinic transition of a long-lived mesoscale convective vortex. *Mon. Wea. Rev.*, **137**, 562–584.
- Grell, G. A., J. Dudhia, and D. R. Stauffer, 1994: A description of the fifth-generation Penn State–NCAR mesoscale model (MM5). NCAR Tech. Note NCAR/TN-398+STR, 117 pp.
- Hertenstein, R. F. A., and W. H. Schubert, 1991: Potential vorticity anomalies associated with squall lines. *Mon. Wea. Rev.*, **119**, 1663–1672.
- Holton, J. R., 2004: *An Introduction to Dynamic Meteorology*. Elsevier, 535 pp.
- Hoskins, B. J., 1976: Baroclinic waves and frontogenesis. Part I: Introduction and Eady waves. *Quart. J. Roy. Meteor. Soc.*, **102**, 103–122.
- Houze, R. A., Jr., 2004: Mesoscale convective systems. *Rev. Geophys.*, **42**, RG4003, doi:10.1029/2004RG000150.
- Jiang, H., and D. J. Raymond, 1995: Simulation of a mature mesoscale convective system using a nonlinear balance model. *J. Atmos. Sci.*, **52**, 161–175.
- Montgomery, M. T., and B. F. Farrell, 1991: Moist surface frontogenesis associated with interior potential vorticity anomalies in a semigeostrophic model. *J. Atmos. Sci.*, **48**, 343–367.
- , and —, 1992: Polar low dynamics. *J. Atmos. Sci.*, **49**, 2484–2505.
- , and R. J. Kallenbach, 1997: A theory for vortex Rossby waves and its application to spiral bands and intensity changes in hurricanes. *Quart. J. Roy. Meteor. Soc.*, **123**, 435–465.
- Moore, R. W., and M. T. Montgomery, 2004: Reexamining the dynamics of short-scale, diabatic Rossby waves, and their role in midlatitude moist cyclogenesis. *J. Atmos. Sci.*, **61**, 754–768.
- , and —, 2005: Analysis of an idealized, three-dimensional diabatic Rossby vortex: A coherent structure of the moist baroclinic atmosphere. *J. Atmos. Sci.*, **62**, 2703–2725.
- , —, and H. C. Davies, 2008: The integral role of a diabatic Rossby vortex in a heavy snowfall event. *Mon. Wea. Rev.*, **136**, 1878–1897.
- Norquist, D. C., E. E. Recker, and R. J. Reed, 1977: The energetics of African wave disturbances as observed during phase III of GATE. *Mon. Wea. Rev.*, **105**, 334–342.
- Raymond, D. J., and H. Jiang, 1990: A theory for long-lived mesoscale convective systems. *J. Atmos. Sci.*, **47**, 3067–3077.
- Snyder, C., and R. S. Lindzen, 1991: Quasi-geostrophic wave-CISK in an unbounded baroclinic shear. *J. Atmos. Sci.*, **48**, 76–86.
- Trier, S. B., W. C. Skamarock, and M. A. LeMone, 1997: Structure and evolution of the 22 February 1993 TOGA COARE squall line: Organization mechanisms inferred from numerical simulation. *J. Atmos. Sci.*, **54**, 386–407.
- , C. A. Davis, and W. C. Skamarock, 2000: Long-lived mesoconvective vortices and their environment. Part I: Observations from the central United States during the 1998 warm season. *Mon. Wea. Rev.*, **128**, 3376–3395.
- Whitaker, J. S., and C. A. Davis, 1994: Cyclogenesis in a saturated environment. *J. Atmos. Sci.*, **51**, 889–907.